A data-driven analysis of inhomogeneous wave field based on two-dimensional Hilbert-Huang transform

Xuanting Hao[a], Lian Shen[a,*]

[a]*St. Anthony Falls Laboratory and Department of Mechanical Engineering, University of Minnesota, Minneapolis, MN, 55455, USA*

Abstract

Quantitative characterization of the wave field nearshore is critical for coastal applications. The spatial inhomogeneity of the coastal wave field poses challenges to conventional Fourier analysis. To address this issue, we propose a data-driven analysis framework based on the adaptive two-dimensional Hilbert–Huang transform, the accuracy of which is first demonstrated using synthetic wave data. We then conduct wave-phase-resolved simulations based on a high-order spectral method, where the initial wave conditions are constructed for sea states with various wave field properties and the bathymetry profile varies continuously from deep water to shallow water. The impact of varying bathymetry is observed on the raw data obtained from the simulation and the large-scale components obtained from the empirical mode decomposition of the raw data. We also calculate the Hilbert spectrum and identify the features of coastal wave processes including refraction, shoaling and breaking. We propose three integral quantities to characterize the spatially-variant wave field, including the direction angle, the characteristic wavenumber, and the wave energy. Further discussions on the limitations of the conventional Fourier analysis and the Hilbert–Huang transform are also provided.

Keywords: Hilbert-Huang transform, modal decomposition, wave-bottom interaction, shoaling waves, wave simulation

*Corresponding author
Email address: shen@umn.edu (Lian Shen)

1. Introduction

Coastal waves are an essential component of the nearshore environment and has a broad range of interactions with human activities [1]. Compared with waves in the open ocean, coastal waves are shaped by the bathymetry in their properties including the amplitude, the propagation direction, and the wavenumber, which are key input parameters in swash flow simulation [2], rip current prediction [3], wave energy converter power calculation [4], and the models in air–sea interactions [5]. The process of acquiring the local wave properties from observed wave data, i.e. wave characterization, is a critical component of the retrieval algorithm in remote sensing, where Fourier analysis has traditionally been used to separate wave motions of different length scales. However, the wave field in coastal region is spatially inhomogeneous due to various physical processes, such as wave shoaling, refraction, and depth-induced breaking. When a physical process, such as wave–current interaction, results in spatial inhomogeneity for short waves, the Fourier transform can be applied to a moving domain for addressing the inhomogeneity and extracting the wave properties. For the wave–bathymetry interaction, however, because its primary impact leads to the spatial variations in long waves, the Fourier transform on a moving domain is less applicable. Consequently, there is a need to develop a data analysis tool capable of addressing the spatial inhomogeneity for the characterization of coastal waves.

Spatial wave data can be obtained from measurement using remote sensing and from numerical simulation using phase-resolved algorithms. Compared with wave buoys that directly record the wave surface elevation and velocity, typical remote sensing techniques using marine radars measure the electromagnetic signals reflected by the ocean surface, and thus the measured raw signal is a complex function of the kinematic quantities [6]. For numerical approaches based on the Navier–Stokes equations, while the wave kinematic data can be readily obtained, it is challenging to simultaneously achieve a kilometer-scale domain size and a meter-scale resolution as in a typical marine radar dataset

because of the high computational cost. To date, direct numerical simulations are limited to mechanistic study and model development using relatively simple wave settings such as monochromatic waves and solitary waves [7, 8, 9, 10]. Another representative numerical tool is the Boussinesq-type models, first proposed for the weakly dispersive waves in shallow water [11]. Modern Boussinesq models have been greatly expanded to account for physical effects such as strong dispersion and nonlinearity [12, 13]. While turbulence is not resolved, the Boussniesq models are more feasible to use for coastal applications than the Navier–Stokes equations because of the relatively low computational cost. Complete reviews on the Boussinesq models can be found in [14] and [15]. A third typical wave model is based on the high-order perturbation expansion of the Zakharov formulation of surface waves [16], i.e., the high-order spectral (HOS) method [17, 18], which has been extended to waves over varying bottoms [19] and gravity–capillary waves [20, 21]. The potential flow assumption in the HOS method is not a prerequisite in some Boussinesq models [14]. Furthermore, the periodic boundary condition is imposed in the HOS method because the linear terms are calculated in the spectral space. However, the HOS method is less restrictive in terms of the weakly dispersion assumption and is computationally more efficient than the Boussinesq models. Because the present study focuses on the wave data analysis, it would be helpful to choose a wave model that can obtain the high-resolution spatial distribution of wave surface elevation and velocity at a relatively low computational cost and the HOS method is thus used for this purpose.

The Hilbert–Huang transform (HHT) was developed as an alternative to the Fourier transform for non-stationary time series analysis [22, 23]. The HHT includes two steps, the empirical mode decomposition (EMD) and the Hilbert transform. Unlike Fourier transform that uses the fixed sinusoidal function as the decomposition basis, the EMD is completely data-driven and a basis function is not required. The Hilbert transform is used for extracting the instantaneous frequency and the spectral distribution of the local wave energy. The HHT has been used in various applications in geophysics with spatial inhomogeneity

and local events [24]. It should be noted that most of these applications are based on the one-dimensional (1D) EMD and Hilbert transform. For applications with two-dimensional (2D) signals, the raw data can be treated as 1D data slices and are analyzed separately using the 1D EMD [25]. This approach, also known as the pseudo-2D EMD, is easy to implement but may cause interslice discontinuity [24]. This limitation can be overcome by using the authentic-2D EMD [26, 27, 28, 29]. [30] applied 2D EMD to streamwise-velocity fluctuations in a turbulent flow over a spanwise oscillatory wall. From the EMD components, they identified the modulation effect of large-scale motions on near-wall small-scale motions. By applying the 2D EMD to the velocity fluctuations in three directions in a turbulent channel flow, [31] observed self-similarity in wall-normal and spanwise directions and substantiated the attached-eddy theory. The Hilbert transform has also been extended to 2D scenarios [32, 33]. A typical application of the 2D HHT is the fringe pattern analysis in optical metrology to extract the physical information from the measured images. For instance, [34] tested the accuracy of the EMD by varying the parameters used in the algorithm and compared the 2D HHT result with that obtained by other algorithms including the temporal phase-shifting and the continuous wavelet transform. Recently, [35] used the 2D HHT to quantify the optical phases in digital holographic microscopy, which was found to produce a favorable result over the Fourier-based approach including Fourier transform and continuous wavelet transform.

In this study, we explore the potential application of 2D HHT for extracting coastal wave features. While the 2D HHT has been found valuable in optical metrology measurements, it is unclear whether the same conclusion holds for coastal wave characterization because of the difference in the wave physics between the optical measurement system and the hydrodynamic system. In optical metrology, the input signal is manually designed as a high-frequency carrier wave such that signal demodulation can be easily performed. In coastal applications, however, the physical conditions of the water waves propagating towards the shore are complex and depend on various environmental parame-

ters. To account for this complexity of coastal waves, we simulate broadband wave fields with varying bathymetry using the HOS method to directly capture the wave system evolution in a wave-phase-resolved framework. The remainder of this paper is organized as follows. In Section 2, we introduce the HOS method, the 2D HHT method, and its validation using synthetic wave data. The shoaling wave problem setup and convergence test results are given in Section 3. The HOS-based simulation results and data analysis are presented in Section 4. Conclusions are provided in Section 5.

2. Methodology

2.1. High-order spectral method

In the HOS method [17, 19], the water motions are assumed to be potential flow, and the wave motions are determined by the surface elevation $\eta(x, y, t)$ and the surface velocity potential $\Phi^S(x, y, t) \equiv \Phi(x, y, \eta(x, y, t), t)$, where Φ is the velocity potential. The governing equations are

$$\frac{\partial \eta}{\partial t} + \nabla\Phi^S \cdot \nabla\eta - (1 + \nabla\eta \cdot \nabla\eta)\frac{\partial \Phi}{\partial z} = 0, \quad z = \eta, \tag{1}$$

$$\frac{\partial \Phi^S}{\partial t} + g\eta + \frac{1}{2}\nabla\Phi^S \cdot \nabla\Phi^S - \frac{1}{2}(1 + \nabla\eta \cdot \nabla\eta)\left(\frac{\partial \Phi}{\partial z}\right)^2 = 0, \quad z = \eta, \tag{2}$$

where $\nabla \equiv (\partial/\partial x, \partial/\partial y)$ is the gradient operator in horizontal directions.

Note that Eqs (1) and (2) are essentially the kinematic and dynamic boundary conditions at the surface, while the kinematic boundary condition at the bottom becomes

$$\Phi_z - \nabla\eta_b \cdot \nabla\Phi = 0, \quad z = -\bar{h} + \eta_b(x, y), \tag{3}$$

where $\bar{h}$ is the mean water depth and $\eta_b(x, y)$ is the bottom bathymetry elevation.

The velocity potential can be written as a perturbation series with respect to wave steepness

$$\Phi(\boldsymbol{x}, z, t) = \sum_{m=1}^{M} \Phi^m(\boldsymbol{x}, z, t), \ -\bar{h} + \eta_b \le z \le \eta. \tag{4}$$

Each perturbation term in the series is expressed as a Taylor series expansion about the mean water surface $z = 0$, and one can get the surface velocity potential

$$\Phi^S(x,y,t) = \sum_{m=1}^{M} \sum_{l=0}^{M-m} \frac{\eta^l}{l!} \frac{\partial^l \Phi^m}{\partial z^l}\bigg|_{z=0}. \tag{5}$$

To satisfy the boundary conditions at the mean bottom and the mean surface simultaneously, the m-th order velocity potential is written as the sum of eigenfunctions

$$\Phi^m(x,y,t) = \beta_0^m z + \sum_{n=1}^{N} \left[\alpha_n^m \frac{\cosh k_n(z+\bar{h})}{\cosh k_n \bar{h}} + \beta_n^m \frac{\sinh k_n(z+\bar{h})}{k_n \cosh k_n \bar{h}} \right] e^{i\boldsymbol{k_n}\cdot\boldsymbol{x}}. \tag{6}$$

Consequently, the surface boundary condition can be written as a boundary-value problem

$$\Phi_{z=0}^{(1)} = \Phi^S, \tag{7}$$

$$\Phi_{z=0}^{(m)} = -\sum_{l=1}^{m-1} \frac{\eta^l}{l!} \frac{\partial^l}{\partial z^l} \Phi^{m-l}\bigg|_{z=0}, \quad m = 2, \cdots, M. \tag{8}$$

The other boundary-value problem arises from the bottom boundary condition

$$\Phi_{z=-\bar{h}}^{(1)} = 0, \tag{9}$$

$$\Phi_{z=-\bar{h}}^{(m)} = -\sum_{l=1}^{m-1} \left[\frac{\partial}{\partial x} \frac{\partial^{l-1}}{\partial z^{l-1}} \Phi_x^{m-l} + \frac{\partial}{\partial y} \frac{\partial^{l-1}}{\partial z^{l-1}} \Phi_y^{m-l} \right], \; m = 2, \cdots, M \tag{10}$$

By solving these two boundary-value problems successively at each perturbation order, one can obtain the values of $\alpha_n^m(t)$ and $\beta_n^m(t)$. Then the vertical velocity at the surface is evaluated as

$$\Phi_z(\mathrm{x},\eta,t) = \sum_{m=1}^{M} \sum_{l=0}^{M-m} \frac{\eta^l}{l!} \frac{\partial^{l+1}}{\partial z^{l+1}} \Phi^m(\mathrm{x},0,t). \tag{11}$$

Here we briefly summarize the numerical scheme of the HOS method. At each time step, the horizontal derivatives of η and Φ^S are first calculated using Fourier transform. The vertical derivative $\partial\Phi/\partial z$ is calculated using the perturbation expansion technique described above. Using the fourth-order Runge–Kutta method, the evolution Eqs (1) and (2) are then advanced in time to obtain

the values of η and Φ^S at the next time step. Because the HOS method is based on the potential flow assumption, wave breaking events are not resolved and the energy dissipation associated with wave breaking is estimated by the combination of an adaptive low-pass filter in the spectral space and a local averaging model in the physical space following [36] and [37]. The low-pass filter removes the high-wavenumber energy

$$\eta_{\mathrm{f}}(\boldsymbol{k}) = \eta(\boldsymbol{k}) \exp[-(k/10k_p)^{12}], \tag{12}$$

$$\Phi^S_{\mathrm{f}}(\boldsymbol{k}) = \Phi^S(\boldsymbol{k}) \exp[-(k/10k_p)^{12}]. \tag{13}$$

where η_{f} and Φ^S_{f} denote the filtered quantities, and k_p is the peak wavenumber determined from the wavenumber spectrum of η. The local averaging model is activated when the local steepness $\sqrt{(\partial\eta/\partial x)^2 + (\partial\eta/\partial y)^2}$ exceeds a threshold, similar to the kinematic criterion of wave breaking. According to [36] and [37], the wave breaking model captures the energy dissipation reasonably well when compared with experimental results [38, 39].

2.2. Two-dimensional Hilbert–Huang transform

We first give a brief overview of the EMD process. In EMD, the raw signal is decomposed into components called intrinsic mode functions (IMF), where each component contains the local oscillating features at different scales. Each IMF is calculated in an iterative sifting process, which is illustrated in Fig. 1. First, the local extrema (i.e., maxima and minima) points are identified from the raw signal $\eta_1(x)$. Then by applying an interpolation algorithm, we can obtain the envelopes corresponding to the extrema points, denoted as $\eta_{1,u}(x)$ and $\eta_{1,l}(x)$. In the 1D sifting process, a cubic spline line is used for generating the envelopes. After the upper and lower envelopes are determined, the updated signal is then calculated by subtracting the mean of the envelopes from the original signal

$$\zeta_1(x) = \eta_1(x) - \frac{1}{2}\left[\eta_{1,u}(x) + \eta_{1,l}(x)\right] \tag{14}$$

The mean of the envelopes is then removed from the obtained signal repeatedly

$$\zeta_{i+1}(x) = \zeta_i(x) - \frac{1}{2}\left[\zeta_{i,u}(x) + \zeta_{i,l}(x)\right], i = 1, 2, \ldots, \tag{15}$$

where $\zeta_{i,u}$ and $\zeta_{i,l}$ are the upper and lower envelopes of ζ_i, respectively.

The sifting process is repeated until the stopping criterion is satisfied, for instance, when the standard deviation error between two consecutive signals in the iteration $\|\zeta_{i+1}(x) - \zeta_i(x)\|$ is less than a threshold. The signal at the final step of the sifting process $\zeta_k(x)$ is the first IMF, which represents an oscillatory mode of the raw signal. In the sifting process, the mean of the envelopes removed from the signal represents the low-wavenumber oscillations of the raw signal, as shown in Fig. 1(b) and (c). Therefore, the IMFs with high-wavenumber oscillations are first extracted in the sifting process, followed by the components with low-wavenumber oscillations. After an IMF is calculated, the residue is calculated by subtracting the IMF from the residue in the previous step

$$\eta_2(x) = \eta_1(x) - \zeta_k(x) \tag{16}$$

and the new residue $\eta_2(x)$ is then used as the input for the next sifting process.

While the overall sifting process is the same in 2D cases, it is more challenging to determine the 2D envelopes, and different implementations of the interpolation algorithms have been proposed, including the surface interpolation by radial basis function [26], cubic interpolation [27], bi-cubic spline interpolation [28], and order statistic filter [29]. Here, we use the order statistic filter because the computational cost is much lower than interpolation methods. The upper and lower envelopes are then calculated by

$$\eta_u(x,y) = \max_{x',y' \in \Omega(x,y)} \eta(x',y') \tag{17}$$

$$\eta_l(x,y) = \min_{x',y' \in \Omega(x,y)} \eta(x',y') \tag{18}$$

where $\Omega(x,y)$ is the filter window centered at (x,y).

The Hilbert transform of a 1D signal $\eta(x)$ is $\boldsymbol{H}[\eta] = (1/\pi) \int \eta(\xi)/(x-\xi) \mathrm{d}\xi$, which is equivalent to a $-\pi/2$ phase shift in the Fourier space. Except for this phase change, $\boldsymbol{H}[\eta]$ preserves the same local amplitude and wavenumber information as the original signal $\eta(x)$. For a two-dimensional signal $\eta(x,y)$,

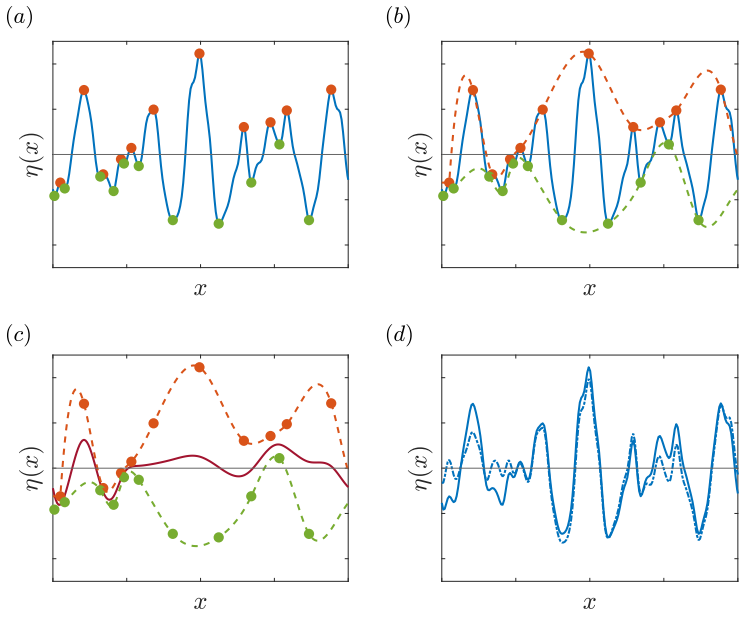

Figure 1: Illustration of the sifting process in EMD: (a) identification of the extrema points (orange and green dots) from the signal, denoted by the blue solid line; (b) interpolation to obtain the envelopes, denoted by the dashed lines; (c) calculation of the mean of the envelopes; (d) calculation of the updated signal, denoted by the blue dash-dot line. For clarity, a 1D case is presented.

the Hilbert transform can be defined as [32]:

$$\boldsymbol{H}[\eta] = -i\exp(-i\theta)\boldsymbol{F}^{-1}\left[\frac{k_x + ik_y}{\sqrt{k_x^2 + k_y^2}}\boldsymbol{F}[\eta]\right]. \tag{19}$$

where k_x and k_y are the wavenumbers in the Fourier space, $\theta(x, y)$ is known as the fringe orientation angle in optical metrology, and $\boldsymbol{F}$ denotes the Fourier transform operator. In the present study, $\theta(x, y)$ denotes the local direction of wave propagation in an irregular wave field.

The main purpose of performing Hilbert transform on a signal is to extract its local properties. Consider a 2D signal varying in space: $\eta(x, y) = A(x, y)\cos\phi(x, y)$, where $A(x, y)$ is the local wave amplitude and $\phi(x, y)$ is the local wave phase (see Fig. 2). It can be shown that these properties are, respec-

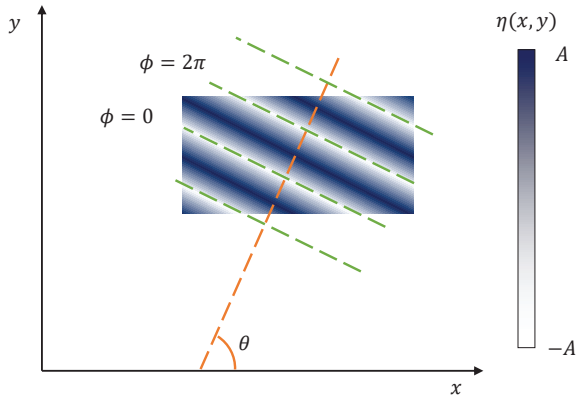

Figure 2: Illustration of a 2D signal $\eta(x, y)$ and the associated local properties, including the amplitude A, the phase ϕ, and the propagating direction θ.

tively:

$$\phi(x, y) = \arctan \frac{|\boldsymbol{H}[\eta]|}{\eta}, \tag{20}$$

$$A(x, y) = \sqrt{|\boldsymbol{H}[\eta]|^2 + \eta^2}, \tag{21}$$

$$(k_x, k_y) = (\frac{\partial \phi}{\partial x}, \frac{\partial \phi}{\partial y}). \tag{22}$$

While the values of θ can be related to the local wavenumber by $\theta = \arctan(k_y/k_x)$, in this study, we use an algorithm proposed by [40]:

$$\theta(x, y) = \frac{1}{2} \arctan \frac{2\widehat{I_x I_y}}{I_y^2 - I_x^2}, \tag{23}$$

$$I_x = \frac{\widehat{y\eta}}{\widehat{y^2}}, \tag{24}$$

$$I_y = \frac{\widehat{x\eta}}{\widehat{x^2}}, \tag{25}$$

where $\widehat{\cdots}$ denotes the averaging in a local rectangle window. Because the local averaging is equivalent to an integral operator, the numerical oscillations caused by possible high-wavenumber noise and insufficient resolutions can be eliminated.

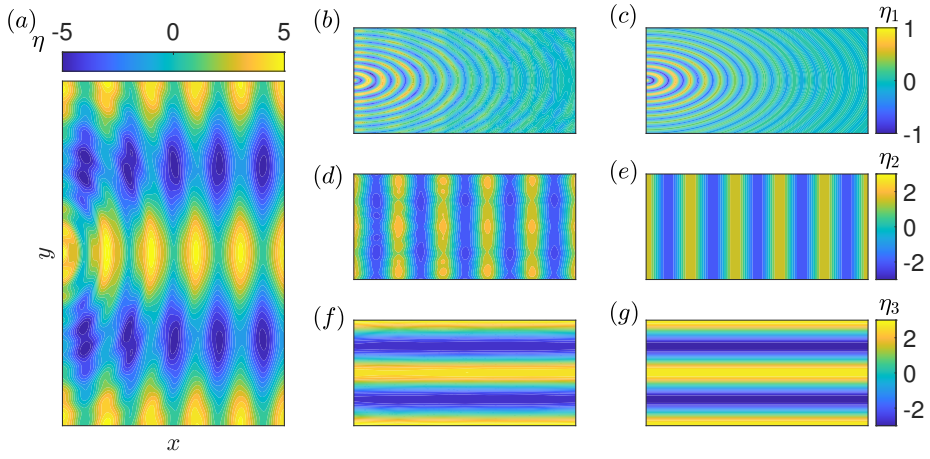

Figure 3: (a) Raw signal $\eta(x, y)$; (b), (d), (f), components calculated using EMD; (c), (e), (g), theoretical components η_1, η_2, η_3.

2.3. Validation with synthetic wave field

To validate the 2D EMD algorithm, we generate a synthetic wave field consisting of three components

$$\eta(x, y) = \eta_1 + \eta_2 + \eta_3, \tag{26}$$

$$\eta_1 = \exp(-0.4r)\cos(15r), \ r = \sqrt{x^2 + (y - \pi)^2}, \tag{27}$$

$$\eta_2 = 2\cos(5x), \tag{28}$$

$$\eta_3 = 3\cos(2y). \tag{29}$$

The inhomogeneity of η is caused by the space-varying amplitude of η_1, while η_2 and η_3 are homogeneous monochromatic waves with constant amplitudes. The raw signal and the decomposition result are shown in Fig. 3. The magnitude and phase of the components extracted by the EMD algorithm are consistent with the theoretical values, except for slight mode mixing of η_1 and η_2 shown in Fig. 3(b) and (d).

We then conduct a second test on the 2D Hilbert transform using a synthetic

wave field. Consider the following wave field in a domain $0 \leq x \leq 2\pi$, $0 \leq y \leq 2\pi$

$$\eta(x, y) = \exp(-0.4r)\cos(15r), \tag{30}$$

$$r = \sqrt{x^2 + (y - \pi)^2}. \tag{31}$$

Here η approximates the wave field generated by an oscillating point source. Substituting η into Equation (19), we can obtain the theoretical values of the amplitude, phase, and direction angle

$$A(x, y) = \exp(-0.4r), \tag{32}$$

$$\phi(x, y) = \arctan\frac{\sin(15r)}{\cos(15r)}, \tag{33}$$

$$\theta(x, y) = \arctan\frac{y - \pi}{x}. \tag{34}$$

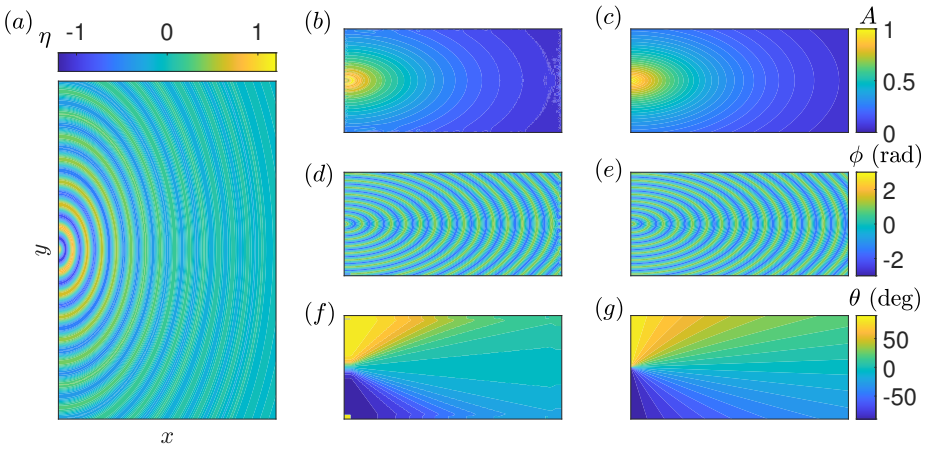

Figure 4: Contours of (a) the original signal $\eta(x, y)$; results of Hilbert transform, including (b) amplitude A, (d) phase ϕ, and (f) direction angle θ; theoretical values of (c) A, (e) ϕ, and (g) θ.

The computed results and the theoretical results are shown in Fig. 4, which are consistent in most part of the region except for near the boundaries. The discrepancies may be partly due to the Fourier transform in Equation (19) conducted for a nonperiodic signal. Besides, the integrations in Equations (24) and (25) are calculated in rectangular windows with a finite size. At the boundaries, the information of the wave field is incomplete for such integrations. While

the boundary effects due to the nonperiodicity and the finite domain size always exist in a realistic wave field, their impact can be reduced by increasing the measurement/simulation domain size such that the region of interest is far from the boundaries. To summarize, the tests using the synthetic wave fields demonstrate the effectiveness of the 2D EMD algorithm and the 2D Hilbert transform in separating wave components of different wavenumbers and extracting the local wave properties, respectively.

3. Problem Setup and Convergence Tests

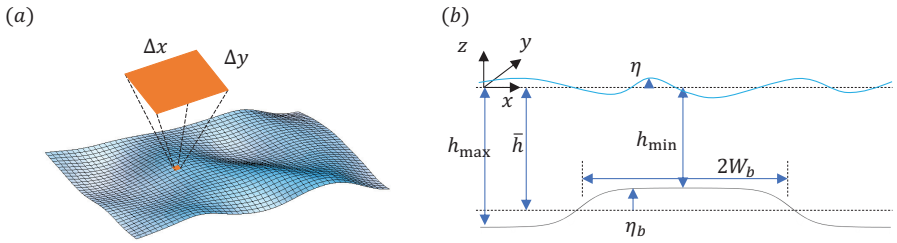

Figure 5: (a) Grid points at the wave surface and (b) sketch of the simulation setting.

We conduct numerical experiments of broadband wave fields propagating over varying water depths. Compared with the synthetic wave fields, the wave fields presented here are simulated using the HOS method capable of capturing nonlinear wave–bottom interactions with the wave phases resolved. The 2D HHT is then applied to the wave fields to obtain the characteristic wave properties. In the numerical experiments, the initial wave field is constructed from the JONSWAP spectrum [41] with directional spreading. The initial phase of each wave component is assigned a random number. The peak wave frequency is $f_p = 0.161$ Hz and the Phillips parameter [42] is set to $\alpha_p = 0.01$. The directional spreading function of the initial wave field is assumed to be

$$D(\Theta) = \frac{1}{\sqrt{\pi}} \frac{\Gamma(N/2+1)}{\Gamma(N/2+1/2)} \cos^N \Theta, \quad |\Theta| \le \frac{\pi}{2} \tag{35}$$

where $D(\Theta)$ is zero for $|\Theta| > \pi/2$ and N is a control parameter. Note that Θ denotes the propagating direction of a wave component in the initial wave

Table 1: Simulation parameters for the phase-resolved wave simulations using the HOS method. Here, $h_{\max}$ and $h_{\min}$ are the maximum and minimum water depth, respectively; W_b is the length of the shallow water region; N is the control parameter of the directional spreading function; L_x and L_y are the computational domain size; N_x and N_y are the grid numbers. All length scales are normalized by the initial peak wavenumber k_p and wave length λ_p.

Case	$k_p h_{\max}$	$k_p h_{\min}$	W_b/λ_p	N	L_x/λ_p	L_y/λ_p	N_x	N_y
WS1L1	1.98	0.256	12.7	2	40	20	2048	1024
WS1L2	1.98	0.256	12.7	2	50	25	2048	1024
WS1L3	1.98	0.256	12.7	2	60	30	2048	1024
WS1L4	1.98	0.256	12.7	2	70	35	2048	1024
WS1L4B2	1.98	0.256	8.3	2	70	35	2048	1024
WS1L4B3	1.98	0.256	17	2	70	35	2048	1024
WS2L4	1.98	0.256	12.7	4	70	35	2048	1024
WS3L5	1.98	0.256	12.7	10	140	35	4096	1024
WS4L5	1.98	0.256	12.7	50	140	35	4096	1024

spectrum, while θ denotes the local wave propagation direction in the physical space as defined in Equation (23). Their values are identical only when the wave field is strictly monochromatic. The bathymetry is a typical smooth and continuous function that has been used in theoretical and numerical studies on wave–bottom interaction [43, 44]

$$\eta_b(x,y) = -C_1 + C_2 \tanh\left[\frac{1}{C_3}(x - \frac{L_x}{2} + W_b)\right], \ 0 \le x \le \frac{L_x}{2} \tag{36}$$

where $C_1 = 20$ m and $C_2 = 8.25$ m are coefficients to determine the maximum and minimum water depths, $C_3 = 60$ m is a coefficient related to the bathymetry slope, and W_b determines the length of the shallow water region. Following [19, 45], the shape of bathymetry is symmetric with respect to $L_x/2$, i.e. $\eta_b(x,y) = \eta_b(L_x - x, y)$, to satisfy the periodic boundary conditions required by the HOS method (see Fig. 5)

The physical and numerical parameters are listed in Table 1. The first six cases are designed to investigate the effects of the computational domain size

L_x and the shallow water region length W_b. For these cases, the value of N is fixed so that directional spreadings of the initial wave field are the same. The cases used for detailed data analysis are WS1L4, WS2L4, WS3L5, and WS4L5, where each case features a different value of the directional spreading index N. The water depths are designed following the criterion based on the wavelength [46]. For the peak wave, the value of $k_p h_{\min} < \pi/10$ is in the shallow water limit, and $k_p h_{\max} = 1.98$ is in the intermediate depth, which is close to the deep water limit $k_p h = \pi$ because the error caused by assuming $\tanh(k_p h_{\max}) = 1$ is less than 4%. The maximal local slope of the bathymetry, i.e., $\max(\partial \eta_b / \partial x)$, is 0.014. The spatial resolution ranges from 1.2 m to 2.1 m in both the x and y directions, comparable to that of marine radars used in field measurements [47, 48]. While it has become possible for the polarimetric slope sensing measurement of surface waves in the gravity–capillary range [49, 50], it would be computationally too expensive to capture the wave dynamics at such a high resolution in our simulations. Besides, for the shortest waves at the present meter-scale-resolution, we expect the direct effect of bathymetry variation to be negligible. The wave simulation duration is $25T_p$ with a time step of $0.025T_p$, and the data for analysis is collected at a sampling interval of $0.1T_p$. The total computational cost is approximately 2.9×10^4 processor hours.

While the mode mixing and boundary effects of 2D HHT is trivial in the analysis of the synthetic data (Fig. 3 and Fig. 4), their impact may not be neglected for the broadband wave field with more wave components. To improve the robustness of the HHT result, a commonly used approach is by manually adding a random signal, typically white noise, to the raw data to form a group of perturbed data sets and then conducting EMD on each artificial data set. The final results, such as the instantaneous frequency and wavenumber, are then calculated from the ensemble average of the results calculated from the artificially perturbed data [51]. In the present study, instead of generating the artificial data sets using this technique, we conduct ten ensemble simulations for each case by varying the random wave phase in the initial condition to obtain genuine wave data sets and then the similar ensemble average is conducted after

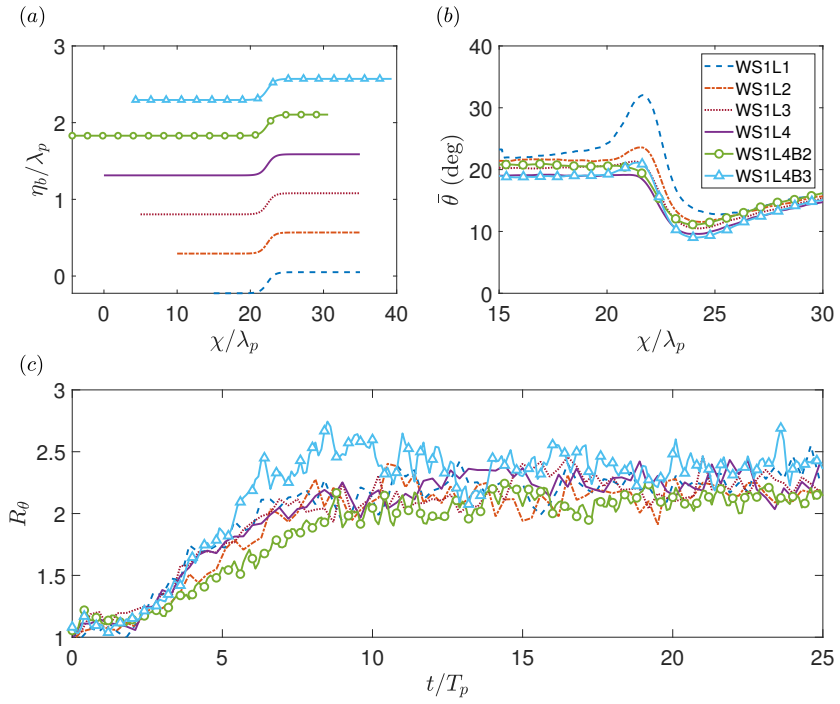

Figure 6: (a) Geometric shapes of the bathymetry, (b) y-averaged direction angle $\bar{\theta}$ calculated using the surface elevation, (c) time history of the ratio $R_\theta = \bar{\theta}(\chi = 20\lambda_p)/\bar{\theta}(\chi = 25\lambda_p)$. Each successive bathymetry profile in (a) is raised by $0.5\lambda_p$ above the preceding curve for clarity.

each data set is analyzed using HHT.

In the following analysis, we introduce an integral variable, i.e., the y-averaged direction angle, defined as

$$\bar{\theta} = \frac{1}{L_y}\int_0^{L_y} |\theta(x,y)|\,\mathrm{d}y. \tag{37}$$

The magnitude of $\bar{\theta}$ is then an average measure of the wave propagation oblique angle at a given water depth.

To determine whether the values of the computational domain size and bathymetry length are appropriate, we conduct a convergence test on the first six cases in Table 1, where the initial wave fields have the same directional spreading index $N = 2$. The geometric shapes of the bathymetry are shown in Fig. 6(a). For comparison, the original coordinate x are adjusted to $\chi = x - x_b$,

where x_b is chosen so that the locations of the bathymetry step in all six cases are the same. The y-averaged direction angle $\bar{\theta}$ is shown in Fig. 6(b). In case WS1L1 and WS1L2, we observe a sudden increase of $\bar{\theta}$ near the end of the bathymetry step $\chi \approx 22\lambda_p$ (see Fig. 6a), which is related to the insufficient domain size. For other cases, the values of $\bar{\theta}$ are largely the same. Fig. 6(c) shows the ratio of the direction angle in the deep water region to that in the shallow water region, defined as $R_\theta = \bar{\theta}(\chi = 20\lambda_p)/\bar{\theta}(\chi = 25\lambda_p)$. Overall, in all cases, the values of R_θ see a similar growth from the initial value of 1 to a steady value around 2 except for slight deviations in case WS1L4B2 and WS1L4B3.

4. Results

4.1. Instantaneous wave field and wave statistics

In this section, we provide a qualitative overview on the features of the wave field. Fig. 7 shows the instantaneous surface elevation, the surface velocity in the x direction, and the bottom profile in case WS1L4. Note that in this case with $N = 2$, the directional spreading function $D(\Theta)$ of the initial wave field reduces to the well-known $\cos^2\Theta$ model. The wave patterns denoted by the contours of η and u experience a change at the bathymetry step where the water depth decreases. While the wave pattern change shows some evidence of wave refraction, it is difficult to determine the change in the wavenumber just by direct observation. In case WS4L5 ($N = 50$), most wave energy propagates in the x direction and the wave pattern change is more distinct, as shown in Fig. 8. In particular, sharply increased surface elevation and velocity are observed near $\chi = 23\lambda_p$ and shorter waves are observed in the shallow water. This phenomenon can be seen as a breaking event because the location of the maximum velocity coincides with the wave crest, known as the kinematic breaking criteria [52]. Unlike case WS1L4, wave refraction is indistinguishable in Fig. 8 because the incoming wave field has a much narrower spreading distribution. In both cases, the contour shape of the surface elevation is qualitatively similar to that of the velocity.

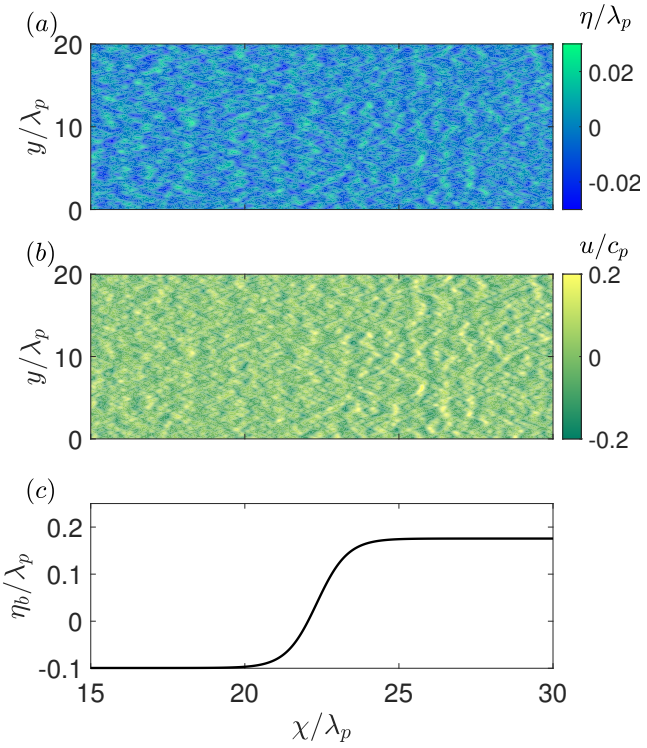

Figure 7: (a) Instantaneous surface elevation; (b) instantaneous surface velocity in the x direction;(c) bottom profile of case WS1L4. All quantities are normalized by the initial peak wave properties. For clarity, only part of the wave field is presented.

We calculate two important wave statistics, the skewness and kurtosis, in the regions with the maximum water depth (hereafter deep water) and the minium water depth (hereafter shallow water). The skewness and kurtosis are defined as $C_3 = \langle(\eta - \langle\eta\rangle)^3\rangle/\sigma_\eta^3$ and $C_4 = \langle(\eta - \langle\eta\rangle)^4\rangle/\sigma_\eta^4$, respectively. Here, $\sigma_\eta = \langle(\eta - \langle\eta\rangle)^2\rangle^{1/2}$ is the standard deviation. For a standard normal distribution, $C_3 = 0$ and $C_4 = 3$. As listed in Table 2, the values of skewness and kurtosis increase significantly with the decreasing water depth. The increase of skewness indicates a more asymmetric wave shape caused by shoaling [53, 54]. The refraction may have also contributed to the change in the skewness. The increase of kurtosis suggests the stronger nonlinear bound-wave dynamics in the shallow water region. In case WS1L4 and WS2L4, the deviations of the statis-

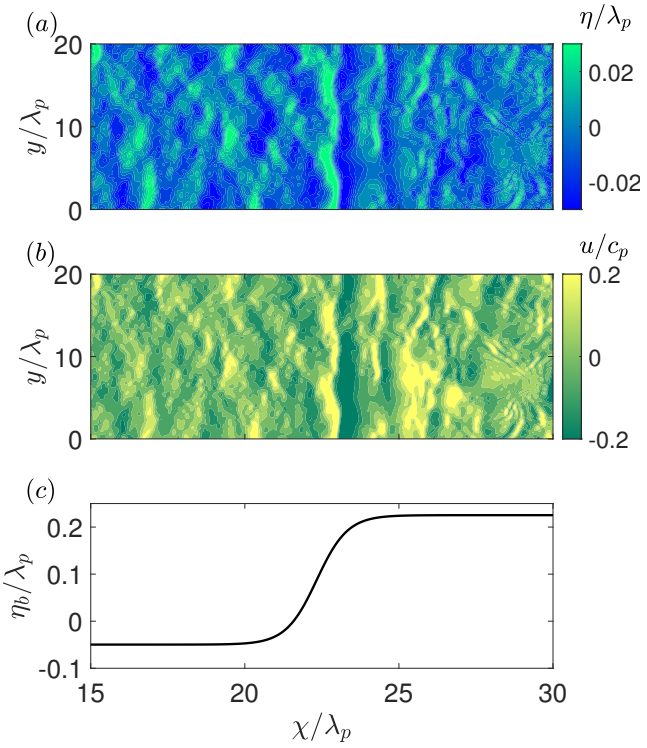

Figure 8: Same as Fig. 7, but for case WS4L5.

tics in the deep water region ($C_{3,D}$ and $C_{4,D}$) from the normal distribution are relatively small, whereas in case WS3L5 and WS4L5 such deviations become noticeable. Here the negative excess kurtosis might be caused by the calculation in a localized region of limited size. In a tank experiment where directional JONSWAP waves were generated [55], several local values of kurtosis were also found to be smaller than three (i.e. negative excess kurtosis). Additionally, in case WS4L5, the spreading index N is large such that the wave dynamics are similar to those in a one-dimensional narrowband wave field (comparing Fig. 7 and Fig. 8), in which the nonlinear resonant wave interaction may contribute to a negative excess dynamic kurtosis [56]. In the shallow water region, for all cases, the deviation of skewness from zero and the deviation of kurtosis from three are significant, indicating strong nonlinearity. The statistics are similar

Table 2: Skewness and kurtosis calculated in the deep-water region $15 < \chi/\lambda_p < 20$ (denoted by the subscript D) and shallow-water region $25 < \chi/\lambda_p < 30$ (denoted by the subscript S). Note that the values of kurtosis are presented as the exceedance to the kurtosis of the standard normal distribution.

Case	Spreading index N	$C_{3,D}$	$C_{3,S}$	$C_{4,D}-3$	$C_{4,S}-3$
WS1L4	2	0.098	0.38	0.01	0.20
WS2L4	4	0.095	0.41	0.02	0.25
WS3L5	10	0.19	0.32	0.07	0.24
WS4L5	50	0.14	0.31	−0.16	0.22

among different cases and the dependence on the initial spreading index is weak. This is likely a result of the depth-limited effect where the wave statistics are dominated by short waves generated after breaking occurs.

4.2. Characteristic wave direction angle

Fig. 9 shows the spatial variation of $\bar{\theta}$ following Equation (37) in four cases with different initial spreading index. The raw data used for computation are the surface elevation η and the surface velocity u, v, and w. For case WS1L4 ($N = 2$) and WS2L4 ($N = 4$), the direction angles calculated from the above four variables have the same spatial distribution, qualitatively. However, their magnitudes are different. In particular, the difference between $\bar{\theta}_w$ and $\bar{\theta}_\eta$ is notably smaller than that between $\bar{\theta}_u$, $\bar{\theta}_v$ and $\bar{\theta}_\eta$. This phenomenon can be explained using the relation of the vertical velocity to the surface elevation via the kinematic condition $w = \partial\eta/\partial t + u\partial\eta/\partial x + v\partial\eta/\partial y$, which reduces to $w = \partial\eta/\partial t$ neglecting the nonlinear terms of high order. Because the resulting operator $\partial/\partial t$ is linear, the distribution of $\bar{\theta}_w$ resembles that of $\bar{\theta}_\eta$. In contrast, there is no explicit formula that connects the horizontal surface velocity components to the surface elevation. For cases WS3L5 ($N = 10$) and WS4L5 ($N = 50$), the spatial variations in $\bar{\theta}_u$, $\bar{\theta}_w$, and $\bar{\theta}_\eta$ are close, because of the relatively weak refraction effect associated with the larger values of N. In all cases, since the directional spreading of the initial wave energy is anisotropic,

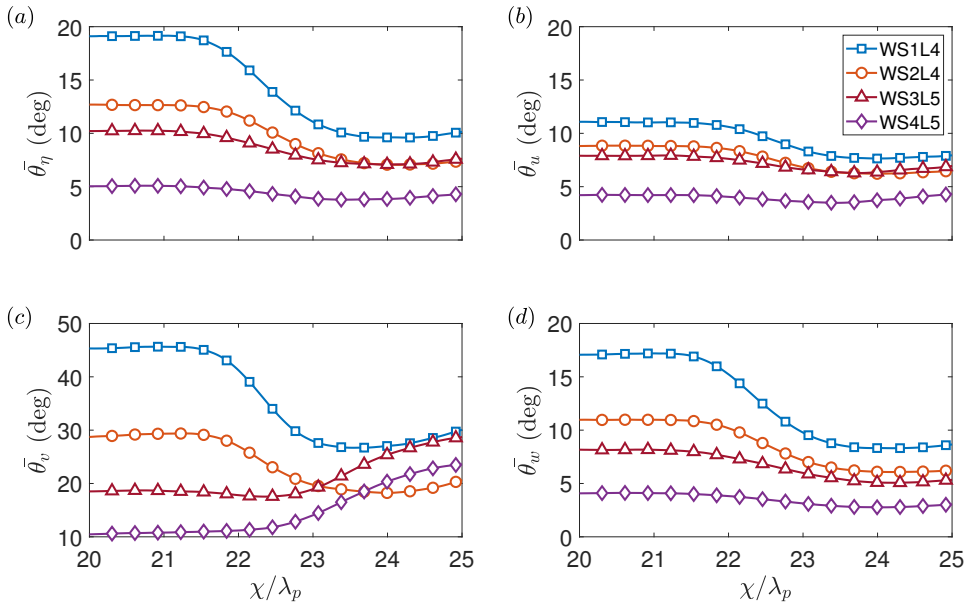

Figure 9: Spatial distribution of $\bar{\theta}$ along the χ direction. Here the subscripts η, u, v, and w denote the raw data used for the calculation. Each case corresponds to an initial directional spreading index: $N = 2$ (WS1L4), $N = 4$ (WS2L4), $N = 10$ (WS3L5), and $N = 50$ (WS4L5).

we observe a significant difference between $\bar{\theta}_u$ and $\bar{\theta}_v$. When the anisotropy is strong (cases WS3L5 and WS4L5), we see an increase of $\bar{\theta}_v$ in the shallow water region, which may be related to the short waves generated by the relatively strong wave breaking events in these two cases.

In applications, the directions of the horizontal coordinates x and y can have different choices, and thus affect the values of $\bar{\theta}_u$ and $\bar{\theta}_v$. On the other hand, the values of η and w are independent of the x and y coordinates since the vertical coordinate is fixed. Changing the directions of horizontal coordinates only leads to an additional constant to the values of $\bar{\theta}_\eta$ and $\bar{\theta}_w$. Therefore, both $\bar{\theta}_\eta$ and $\bar{\theta}_w$ can be used as the characteristic angle of a spatially inhomogeneous directional wave field in the coastal region.

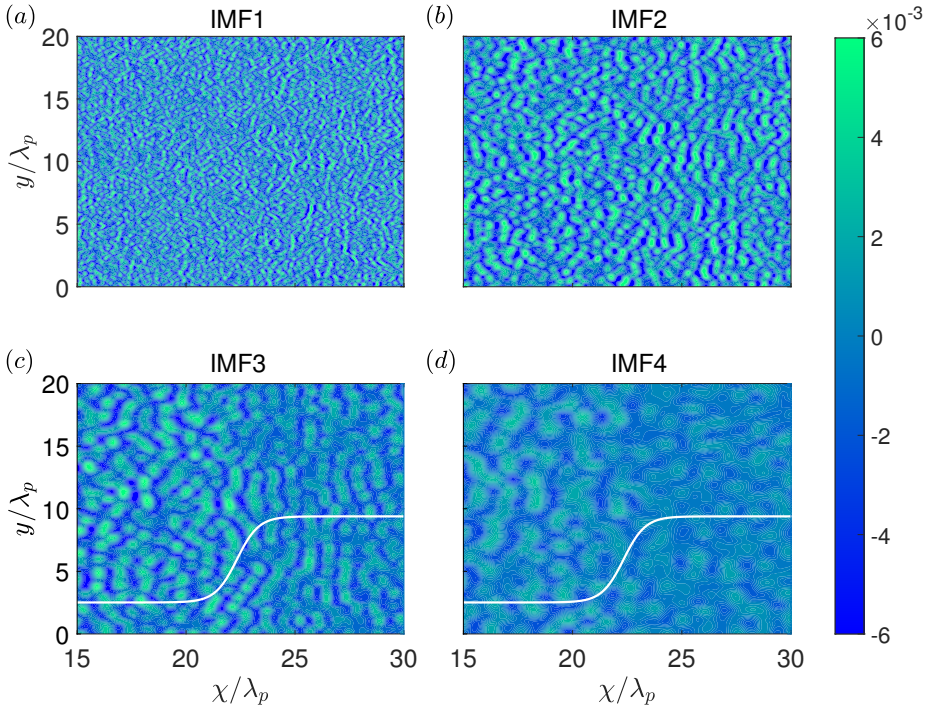

Figure 10: Intrinsic mode functions of the surface elevation. The raw data is the instantaneous surface elevation in a single run of the case WS1L4 (directional spreading index N=2) and the contour values are normalized by λ_p. The bathymetry shape is denoted by the white lines in (c) and (d).

4.3. Intrinsic mode functions and Hilbert spectrum

Following the same process used to decompose the synthetic wave field shown in Fig. 3, we can apply the 2D EMD to the surface elevation and obtain the IMF of the wave field simulated using the HOS method. Fig. 10 and 11 show examples of the first four components of IMF calculated using the surface elevation in cases WS1L4 ($N = 2$) and WS4L5 ($N = 50$), respectively. The component with a pattern of small length scales, IMF1, is first extracted from the raw data by the EMD algorithm, followed by IMF2-IMF4 where the length scales increase gradually. The amplitudes also vary among different IMFs. In both case WS1L4 ($N = 2$) and case WS4L5 ($N = 50$), the spatial distribution of IMF1 is nearly homogeneous, while the contour shapes of IMF3 and IMF4 show noticeable

variations with the water depth change in the region $20 < \chi/\lambda_p < 25$ (see the bathymetry profile in Fig. 7 and 8). Similar to the contour shapes of η shown in Fig. 7 and 8, the directional spreading index N determines the distributions of IMFs in both cases.

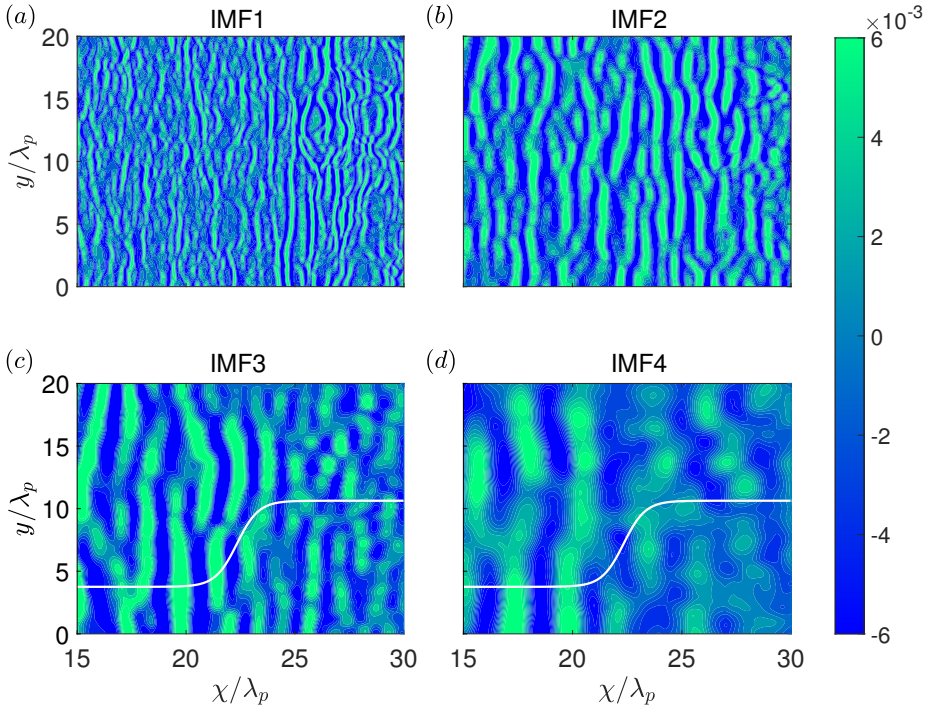

Figure 11: Same as Fig. 10, but for case WS4L5 (directional spreading index $N = 50$).

In contrast to Fourier analysis where each decomposed mode contains strictly a single wave component in the form of sinusoidal functions, each of the IMFs calculated with EMD still contains waves of multiple scales, known as mode mixing [23]. While it is not observed in the analysis of the synthetic wave fields (see Fig. 3), mode mixing is inevitable when EMD is used for analyzing the broadband fields. The mode mixing phenomenon in IMFs can be alleviated by using the ensemble EMD algorithm, according to [24]. In our numerical experiments, the ensemble average is performed after the quantitative features of the IMFs are obtained. Thus, we expect the error induced by the mode

mixing problem to be small.

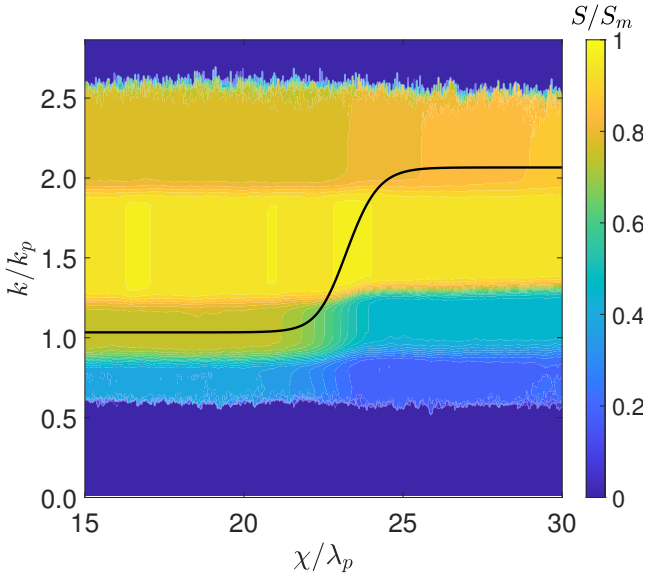

Figure 12: Hilbert amplitude spectrum of the wave field in case WS1L4 (directional spreading index $N = 2$), normalized by its maximal value S_m. The black solid line denotes the theoretical wavenumber change of a monochromatic wave with a deep water wavenumber of $(k_p, 0)$.

The outputs of the EMD algorithm include the local amplitude and instantaneous wavenumber information of the wave field. By plotting the amplitude $A(x, y)$ as a function of the wavenumber and location in the physical space, we obtain the Hilbert amplitude spectrum. For visualization, we define $S = \int A(x, y)dy$, as shown in Fig. 12 and 13. The wave shoaling effect can be observed from the contours of the Hilbert spectrum, as the most energetic part moves from low wavenumbers to high wavenumbers with the decreasing water depth. For comparison, we calculate the wavenumber change of a monochromatic wave propagating in the $+x$ direction based on the linear wave shoaling theory [46]. There is an apparent deviation of the actual dominant wavenumber from the linear prediction because of the physical processes in addition to shoaling, such as refraction. In case WS4L5 where the initial directional spreading index $N = 50$, a region of large amplitudes is observed at the end of

the bathymetry step, and the wave energy decreases significantly as the waves propagate into the shallow water region ($\chi/\lambda_p > 25$), indicating that the local averaging wave breaking model is invoked at the large local steepness (see also Fig. 8b).

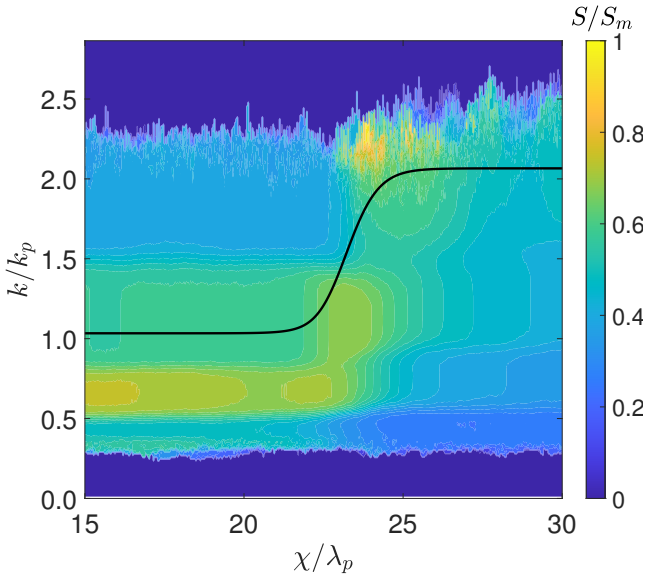

Figure 13: Same as Fig. 12, but for case WS4L5 (directional spreading index $N = 50$).

Based on the Hilbert spectrum, we define the characteristic wavenumber $k_c = \int kSdk / \int Sdk$ and the characteristic energy $\epsilon_c = \int S^2 dk / \int dk$. The spatial distributions of k_c and ϵ_c are shown in Fig. 14(a) and 14(b), respectively. In cases WS1L4 ($N = 2$) and WS2L4 ($N = 4$), the values of k_c see a slight (5%) increase when the water depth reduces, while those in cases WS3L5 ($N = 10$) and WS4L5 ($N = 50$) increase by over 20%. While it is well-known that the amplitude of a monochromatic wave grows in the shoaling process, the characteristic energy in cases WS1L4 and WS2L4 decreases by 15%. This seemingly counter-intuitive phenomenon can be attributed to the dispersion in a complex wave field, which can cause the energy decay of a shoaling wave packet [43]. In cases WS3L5 and WS4L5, the wave fields are nearly unidirectional (see Fig. 11). Therefore, the energy first reaches a peak value due to shoaling and then de-

creases drastically towards the shallow water region after the breaking models are invoked. The spatial variations of k_c and ϵ_c profiles correspond to the qualitative features of the contour patterns described in Section 4.1 (see the instantaneous wave field in Fig. 7 and 8). Fig. 14 also shows that the results of cases WS1L4 ($N = 2$) and WS2L4 ($N = 4$) are largely the same despite the difference in the initial directional spreading index, suggesting that their shoaling strengths are close. On the other hand, the depth-induced increase of k_c and ϵ_c in case WS4L5 is higher than that in case WS3L5 and the locations of their magnitude change are different. It can be inferred that the difference in the initial directional spreading index ($N = 10$ in case WS3L5 and $N = 50$ in case WS4L5) affects the shoaling strength and the breaking onset in these two cases.

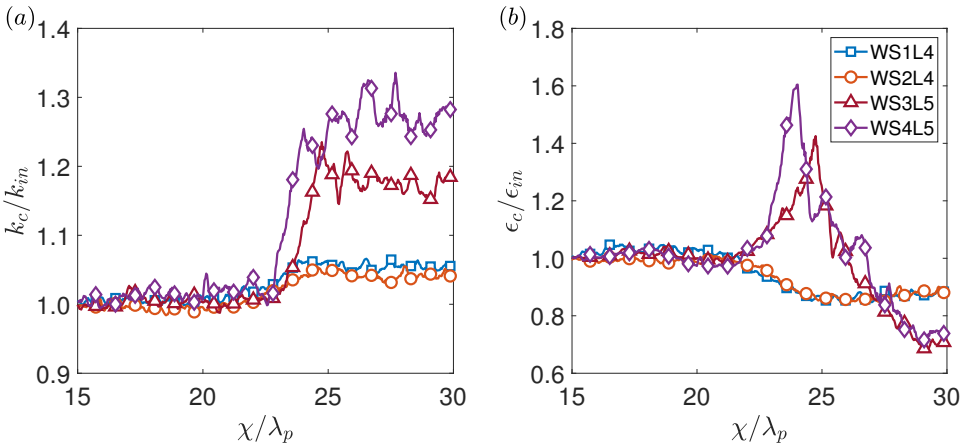

Figure 14: Spatial distribution of (a) the characteristic wavenumber k_c and (b) characteristic wave energy ϵ_c. Both quantities are normalized by the inlet values k_{in} and ϵ_{in} at $\chi/\lambda_p = 15$.

4.4. Discussions

For comparison, we apply the conventional Fourier analysis to the wave field. The wavenumber–frequency spectrum is calculated for the surface elevation in the computational domain. In Fig. 15, we plot the integrated spectrum $E(k_x, \omega) = \int E(k_x, k_y, \omega) dk_y$ and the linear dispersion relation at two water

depths. As shown, a large portion of the wave energy is located beyond the dispersion relation curves, especially in case WS1L4 (Fig. 15a). In the low $k_x - \omega$ region, wave energy scatters between these two curves because large scale waves are directly affected by the depth change. The deviation of the wave energy from the linear dispersion relation has also been reported in the full depth-limited spectrum obtained from field observation [57]. In an extended analysis using the same field data, [58] found that such deviation can cause a significant difference in the directional spreading of the wavenumber and frequency spectra. Another major limitation of the Fourier transform is the implicit assumption that the data is spatially homogeneous. Otherwise, the spatial inhomogeneity can cause spurious numerical oscillations in the spectrum, and this phenomenon is more pronounced in case WS4L5 (Fig. 15b) because of the amplitude increase shown in Fig. 11(a). Unlike the Hilbert spectrum, the Fourier spectrum misses the spatial information of the events occurring in the physical space, because the phase information of the basis functions is usually discarded.

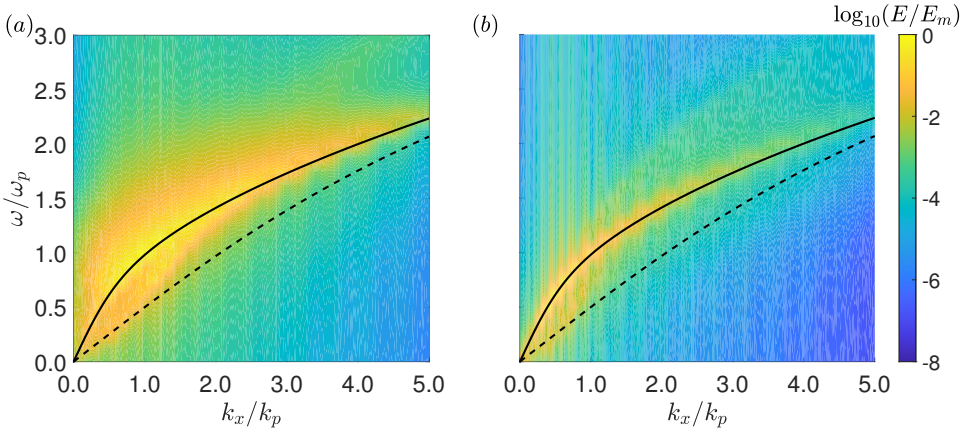

Figure 15: Fourier wavenumber–frequency spectrum in (a) case WS1L4 ($N = 2$) and (b) case WS4L5 ($N = 50$). Here, the black solid line and the dashed line denote the linear wave dispersion relation at depth $h_{\max}$ and $h_{\min}$, respectively.

In general, it is impractical to directly use the data produced by EMD. At first glance, the IMF components generated by the EMD algorithm (Fig. 10 and 11) has a larger degree of freedom than the raw data (Fig. 7 and 8). On

the other hand, a pure data analysis process cannot introduce more physical information to the data itself. This conflict can be explained by the intrinsic correlation among the data in each IMF component. For a Fourier transform, this correlation is more evident, because any Fourier component, regardless of its data size, is uniquely determined by a few parameters: the amplitude, the wavenumber, and the phase. Correspondingly, the characteristic direction angle, wavenumber, and energy presented in Fig. 9 and Fig. 14 provide a reduced-order description of the EMD result, which is useful to reduce the computational cost for feeding the simulation result as inputs to applications. A notable example is the air–sea momentum flux estimation in large-scale models, where the drag coefficient is modeled as a parameterized function of wave features [5].

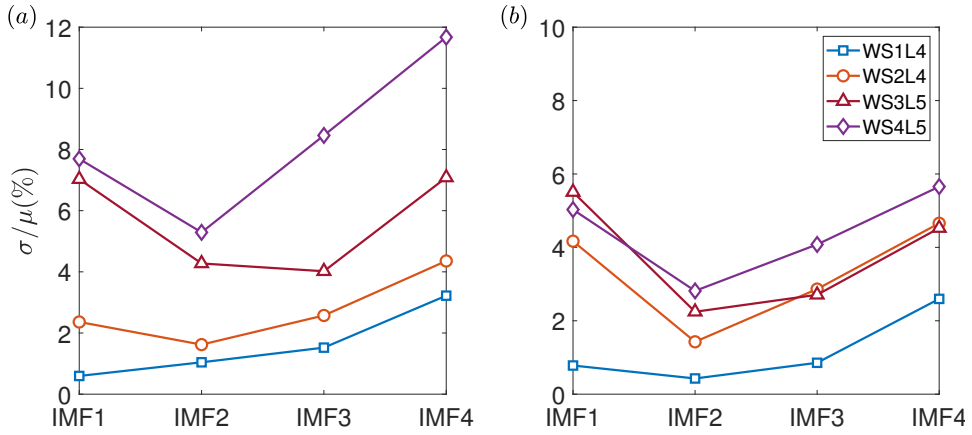

Figure 16: Standard deviation σ of the IMF amplitude, normalized by the mean value μ. The statistics are calculated using: (a) ensemble averaging; (b) time averaging.

Contrary to the Fourier transform which is based on a rigorous mathematical operation, the EMD process is adaptive and flexible. Therefore, the confidence limit of the HHT result depends on the physical condition and the averaging operation. Consider the amplitude of the IMF component $a_{IMF} = (\sum \eta_{IMF}(i,j)^2)^{1/2}$, where i and j denote the index in x and y directions, respectively, and η_{IMF} denotes the IMF component. The mean value $\mu = \mu(a_{IMF})$ and standard deviation $\sigma = \sigma(a_{IMF})$ can be calculated either for all ensemble

cases at a given time (ensemble averaging) or for all time series in one ensemble case (time averaging). In cases WS1L4 ($N = 2$) and WS2L4 ($N = 4$) with weak shoaling and strong refraction, σ is less than 5% of the mean value μ, as shown in Fig. 16. In the other two cases WS3L5 ($N = 10$) and WS4L5 ($N = 50$), the values of σ/μ are larger, especially when calculated using the ensemble averaging. This difference among the four cases may be associated with the breaking-induced randomness, which is apparently stronger in case WS3L5 ($N = 10$) and WS4L5 ($N = 50$). The magnitude of σ is also affected by the initial wave condition of each ensemble case as mentioned in the problem setup in Section 3. In addition to the wave conditions, the adaptive feature of the EMD algorithm is also a cause of the standard deviation because the calculated IMF may contain different components when performing the averaging as shown by [59].

Because the EMD algorithm can decompose the raw data into components of different scales, it can be used as an adaptive filter in the data preprocessing of conventional Fourier analysis. When the inhomogeneity is weak, the Hilbert transform can be replaced by Fourier transform to extract the wave properties. In the analysis of velocity fluctuations in a canonical channel flow, [31] used this approach to separate the turbulence scales. While the computational cost of HHT is higher than the Fourier transform as a result of the algorithms used for 2D envelope construction, the iterative sifting process, and the direction angle calculation, we find a single processor to be sufficiently efficient for post-processing the O(10) terabyte data obtained from our wave simulations.

5. Conclusions

In this study, we have proposed a framework to characterize the inhomogeneous wave field based on an adaptive data analysis method. In this framework, we generalize the original 1D Hilbert–Huang transform to the 2D case by a combination of the 2D EMD algorithm and the 2D Hilbert transform. The EMD algorithm is a sifting process that decomposes the raw data into fundamental

oscillatory modes without a predefined basis function. The Hilbert transform provides an estimation of the local wave properties. We have tested the accuracy of the EMD and Hilbert transform algorithms using synthetic wave fields. We find the EMD algorithm to be effective in separating an inhomogeneous wave field that contains a wave generated by a point source and two monochromatic wave components. Additionally, our test on the Hilbert transform shows that the local wave properties obtained are nearly identical to the analytical solution.

We have performed numerical experiments to examine the performance of the 2D Hilbert–Huang transform in the analysis of more complex wave data with realistic parameters. The phase-resolved HOS method is used to simulate broadband directional wave fields propagating over a coastal bathymetry. In the numerical configurations, we have considered multiple choices of key numerical and physical parameters. A convergence test has been performed to justify the values of the computational domain size, the bathymetry length, and the simulation duration. The bathymetry effect on the wave field is manifested in the contour patterns of the surface elevation and velocity, and the strength of the bathymetry impact varies with the initial directional spreading index. We have identified three wave properties, namely the averaged direction angle $\bar{\theta}$, characteristic wavenumber k_c, and characteristic wave energy ϵ_c, to quantify the inhomogeneous wave field. We find that the direction angles calculated from the surface elevation and the vertical velocity are consistent and can measure the effect of wave refraction. The 2D EMD algorithm is found to be effective in decomposing the raw data into IMFs of different length scales, and the bathymetry effect is observed in the low-wavenumber IMF. We demonstrate the capability of Hilbert spectrum in providing accurate information on the localized events such as the wave energy redistribution caused by shoaling and the amplitude increase prior to wave breakings. In contrast, the conventional Fourier method is unable to capture the spatial variations of wave properties as a result of the nonlinearity and the spatial inhomogeneity.

Finally, we remark that, while our wave data is obtained from the potential-flow-based HOS simulation, the 2D Hilbert–Huang transform can be directly ap-

plied to the analysis of the coastal wave data obtained from other phase-resolved models, e.g., the Boussinesq models. Also, as the remote sensing techniques play an increasingly important role in the high-resolution spatial measurement of the coastal region, our framework can be a useful tool in the postprocessing of these 2D observational data.

Acknowledgments

This work is partially supported by the Office of Naval Research and Minnesota Sea Grant. The authors gratefully acknowledge the referees for their valuable comments.

Declaration of competing interest

The authors declare that they have no known competing financial interests or personal relationships that could have appeared to influence the work reported in this paper.

References

[1] R. G. Dean, R. A. Dalrymple, Coastal processes with engineering applications, Cambridge University Press, 2001.

[2] X. Deng, H. Liu, Z. Jiang, T. E. Baldock, Swash flow properties with bottom resistance based on the method of characteristics, Coast. Eng. 114 (2016) 25–34. doi:10.1016/j.coastaleng.2016.03.012.

[3] J. W. Long, H. Özkan-Haller, Forcing and variability of nonstationary rip currents, J. Geophys. Res. Ocean. 121 (1) (2016) 520–539. doi:10.1002/2015JC010990.

[4] J. A. Oskamp, H. T. Özkan-Haller, Power calculations for a passively tuned point absorber wave energy converter on the Oregon coast, Renew. Energy 45 (2012) 72–77. doi:10.1016/j.renene.2012.02.004.

[5] J. B. Edson, V. Jampana, R. A. Weller, S. P. Bigorre, A. J. Plueddemann, C. W. Fairall, S. D. Miller, L. Mahrt, D. Vickers, H. Hersbach, On the exchange of momentum over the open ocean, J. Phys. Oceanogr. 43 (8) (2013) 1589–1610. doi:10.1175/JPO-D-12-0173.1.

[6] R. Holman, M. C. Haller, Remote sensing of the nearshore, Ann. Rev. Mar. Sci. 5 (1) (2013) 95–113. doi:10.1146/annurev-marine-121211-172408.

[7] P. Lubin, S. Glockner, O. Kimmoun, H. Branger, Numerical study of the hydrodynamics of regular waves breaking over a sloping beach, Eur. J. Mech. - B/Fluids 30 (6) (2011) 552–564. doi:10.1016/j.euromechflu.2011.01.001.

[8] M. Alagan Chella, H. Bihs, D. Myrhaug, M. Muskulus, Breaking characteristics and geometric properties of spilling breakers over slopes, Coast. Eng. 95 (2015) 4–19. doi:10.1016/j.coastaleng.2014.09.003.

[9] S. Gsell, T. Bonometti, D. Astruc, A coupled volume-of-fluid/immersed-boundary method for the study of propagating waves over complex-shaped bottom: application to the solitary wave, Comput. & Fluids 131 (2016) 56–65. doi:10.1016/j.compfluid.2016.03.013.

[10] R. A. R. Roselli, G. Vernengo, S. Brizzolara, R. Guercio, SPH simulation of periodic wave breaking in the surf zone - A detailed fluid dynamic validation, Ocean Eng. 176 (2019) 20–30. doi:10.1016/j.oceaneng.2019.02.013.

[11] J. Boussinesq, Théorie des ondes et des remous qui se propagent le long d'un canal rectangulaire horizontal, en communiquant au liquide contenu dans ce canal des vitesses sensiblement pareilles de la surface au fond, J. Mathématiques Pures Appliquées. Deuxième Série (17) (1872) 55–108.

[12] Z. Liu, K. Fang, A new two-layer Boussinesq model for coastal waves from deep to shallow water: Derivation and analysis, Wave Motion 67 (2016) 1–14. doi:10.1016/j.wavemoti.2016.07.002.

[13] C. Lawrence, D. Adytia, E. van Groesen, Variational Boussinesq model for strongly nonlinear dispersive waves, Wave Motion 76 (2018) 78–102. doi:10.1016/j.wavemoti.2017.10.009.

[14] M. Brocchini, A reasoned overview on Boussinesq-type models: the interplay between physics, mathematics and numerics, Proc. R. Soc. A Math. Phys. Eng. Sci. 469 (2013) 20130496. doi:10.1098/rspa.2013.0496.

[15] J. T. Kirby, Boussinesq models and their application to coastal processes across a wide range of scales, J. Waterw. Port, Coastal, Ocean Eng. 142 (6) (2016) 03116005. doi:10.1061/(ASCE)WW.1943-5460.0000350.

[16] V. E. Zakharov, Stability of periodic waves of finite amplitude on the surface of a deep fluid, J. Appl. Mech. Tech. Phys. 9 (2) (1968) 190–194. doi:10.1007/BF00913182.

[17] D. G. Dommermuth, D. K. P. Yue, A high-order spectral method for the study of nonlinear gravity waves, J. Fluid Mech. 184 (1987) 267–288. doi:10.1017/S002211208700288X.

[18] B. J. West, K. A. Brueckner, R. S. Janda, D. M. Milder, R. L. Milton, A new numerical method for surface hydrodynamics, J. Geophys. Res. Ocean. 92 (C11) (1987) 11803–11824. doi:10.1029/JC092iC11p11803.

[19] Y. Liu, D. K. P. Yue, On generalized Bragg scattering of surface waves by bottom ripples, J. Fluid Mech. 356 (1998) 297–326. doi:10.1017/S0022112097007969.

[20] Y. Pan, D. K. P. Yue, Direct numerical investigation of turbulence of capillary waves, Phys. Rev. Lett. 113 (9) (2014) 094501. doi:10.1103/PhysRevLett.113.094501.

[21] Y. Pan, D. K. P. Yue, Decaying capillary wave turbulence under broad-scale dissipation, J. Fluid Mech. 780 (2015) R1. doi:10.1017/jfm.2015.487.

[22] N. E. Huang, Z. Shen, S. R. Long, M. C. Wu, H. H. Shih, Q. Zheng, N.-C. Yen, C.-C. Tung, H. H. Liu, The empirical mode decomposition and the Hilbert spectrum for nonlinear and non-stationary time series analysis, Proc. R. Soc. A Math. Phys. Eng. Sci. 454 (1971) (1998) 903–995. doi:10.1098/rspa.1998.0193.

[23] N. E. Huang, Z. Shen, S. R. Long, A new view of nonlinear water waves: the Hilbert spectrum, Annu. Rev. Fluid Mech. 31 (1) (1999) 417–457. doi:10.1146/annurev.fluid.31.1.417.

[24] N. E. Huang, Z. Wu, A review on Hilbert-Huang transform: method and its applications to geophysical studies, Rev. Geophys. 46 (2) (2008) 1–23. doi:10.1029/2007RG000228.

[25] S. R. Long, Applications of HHT in image analysis, in: N. E. Huang, S. S. P. Shen (Eds.), Hilbert-Huang Transform Introd. Appl., World Scientific, Singapore, 2005, pp. 289–305. doi:10.1142/9789812703347_0013.

[26] J. C. Nunes, Y. Bouaoune, E. Delechelle, O. Niang, P. Bunel, Image analysis by bidimensional empirical mode decomposition, Image Vis. Comput. 21 (12) (2003) 1019–1026. doi:10.1016/S0262-8856(03)00094-5.

[27] C. Damerval, S. Meignen, V. Perrier, A fast algorithm for bidimensional EMD, IEEE Signal Process. Lett. 12 (10) (2005) 701–704. doi:10.1109/LSP.2005.855548.

[28] Y. Xu, B. Liu, J. Liu, S. Riemenschneider, Two-dimensional empirical mode decomposition by finite elements, Proc. R. Soc. A Math. Phys. Eng. Sci. 462 (2074) (2006) 3081–3096. doi:10.1098/rspa.2006.1700.

[29] M. R. Thirumalaisamy, P. J. Ansell, Fast and adaptive empirical mode decomposition for multidimensional, multivariate signals, IEEE Signal Process. Lett. 25 (10) (2018) 1550–1554. doi:10.1109/LSP.2018.2867335.

[30] L. Agostini, E. Touber, M. A. Leschziner, Spanwise oscillatory wall motion in channel flow: drag-reduction mechanisms inferred from DNS-predicted

phase-wise property variations at Re_τ=1000, J. Fluid Mech. 743 (2014) 606–635. doi:10.1017/jfm.2014.40.

[31] C. Cheng, W. Li, A. Lozano-Durán, H. Liu, Identity of attached eddies in turbulent channel flows with bidimensional empirical mode decomposition, J. Fluid Mech. 870 (2019) 1037–1071. doi:10.1017/jfm.2019.272.

[32] K. G. Larkin, D. J. Bone, M. A. Oldfield, Natural demodulation of two-dimensional fringe patterns. I. General background of the spiral phase quadrature transform, J. Opt. Soc. Am. A 18 (8) (2001) 1862–1870. doi:10.1364/JOSAA.18.001862.

[33] T. Bulow, G. Sommer, Hypercomplex signals - a novel extension of the analytic signal to the multidimensional case, IEEE Trans. Signal Process. 49 (11) (2001) 2844–2852. doi:10.1109/78.960432.

[34] M. Wielgus, K. Patorski, Evaluation of amplitude encoded fringe patterns using the bidimensional empirical mode decomposition and the 2D Hilbert transform generalizations, Appl. Opt. 50 (28) (2011) 5513–5523. doi:10.1364/AO.50.005513.

[35] M. Trusiak, V. Mico, J. Garcia, K. Patorski, Quantitative phase imaging by single-shot Hilbert–Huang phase microscopy, Opt. Lett. 41 (18) (2016) 4344. doi:10.1364/OL.41.004344.

[36] G. Wu, Direct simulation and deterministic prediction of large-scale nonlinear ocean wave-field, Ph.D. thesis, Massachusetts Institute of Technology. (2004).
URL http://hdl.handle.net/1721.1/33450

[37] W. Xiao, Y. Liu, G. Wu, D. K. P. Yue, Rogue wave occurrence and dynamics by direct simulations of nonlinear wave-field evolution, J. Fluid Mech. 720 (2013) 357–392. doi:10.1017/jfm.2013.37.

[38] R. J. Rapp, W. K. Melville, Laboratory measurements of deep-water breaking waves, Philos. Trans. R. Soc. London A Math. Phys. Eng. Sci. 331 (1622) (1990) 735–800.

[39] M. P. Tulin, T. Waseda, Laboratory observations of wave group evolution, including breaking effects, J. Fluid Mech. 378 (1999) 197–232. doi:10.1017/S0022112098003255.

[40] X. Yang, Q. Yu, S. Fu, A combined method for obtaining fringe orientations of ESPI, Opt. Commun. 273 (1) (2007) 60–66. doi:10.1016/j.optcom.2006.12.026.

[41] K. Hasselmann, T. P. Barnett, E. Bouws, H. Carlson, D. E. Cartwright, K. Enke, J. A. Ewing, H. Gienapp, D. E. Hasselmann, P. Kruseman, A. Meerburg, P. Müller, D. J. Olbers, K. Richter, W. Sell, H. Walden, Measurements of wind-wave growth and swell decay during the Joint North Sea Wave Project (JONSWAP), Deutsches Hydrographisches Institut, 1973.

[42] O. M. Phillips, The equilibrium range in the spectrum of wind-generated waves, J. Fluid Mech. 4 (1958) 426–434. doi:10.1017/S0022112058000550.

[43] E. S. Benilov, J. D. Flanagan, C. P. Howlin, Evolution of packets of surface gravity waves over smooth topography, J. Fluid Mech. 533 (3) (2005) 289–301. doi:10.1017/S0022112005004246.

[44] J. Dong, B. Wang, X. Zhao, H. Liu, Wave forces exerted on a submerged horizontal plate over an uneven bottom, J. Eng. Mech. 144 (6) (2018) 04018030. doi:10.1061/(ASCE)EM.1943-7889.0001447.

[45] M.-R. Alam, Y. Liu, D. K. P. Yue, Bragg resonance of waves in a two-layer fluid propagating over bottom ripples. Part II. Numerical simulation, J. Fluid Mech. 624 (2009) 225–253. doi:10.1017/S002211200800548X.

[46] R. G. Dean, R. A. Dalrymple, Water wave mechanics for engineers and scientists, World Scientific, Singapore; Teaneck, NJ, 1991.

[47] B. Lund, H. C. Graber, H. Tamura, C. O. Collins, S. M. Varlamov, A new technique for the retrieval of near-surface vertical current shear from marine X-band radar images, J. Geophys. Res. Ocean. 120 (12) (2015) 8466–8486. doi:10.1002/2015JC010961.

[48] M. Shao, D. G. Ortiz-Suslow, B. K. Haus, B. Lund, N. J. Williams, T. M. Özgökmen, N. J. M. Laxague, J. Horstmann, J. M. Klymak, The variability of winds and fluxes observed near submesoscale fronts, J. Geophys. Res. Ocean. 124 (11) (2019) 7756–7780. doi:10.1029/2019JC015236.

[49] N. J. M. Laxague, B. K. Haus, D. Bogucki, T. Özgökmen, Spectral characterization of fine-scale wind waves using shipboard optical polarimetry, J. Geophys. Res. Ocean. 120 (4) (2015) 3140–3156. doi:10.1002/2014JC010403.

[50] N. J. M. Laxague, C. J. Zappa, D. A. LeBel, M. L. Banner, Spectral characteristics of gravity-capillary waves, with connections to wave growth and microbreaking, J. Geophys. Res. Ocean. 123 (7) (2018) 4576–4592. doi:10.1029/2018JC013859.

[51] Z. Wu, N. E. Huang, Ensemble empirical mode decomposition: a noise-assisted data analysis method, Adv. Adapt. Data Anal. 01 (01) (2009) 1–41. doi:10.1142/S1793536909000047.

[52] M. Perlin, W. Choi, Z. Tian, Breaking waves in deep and intermediate waters, Annu. Rev. Fluid Mech. 45 (1) (2013) 115–145. doi:10.1146/annurev-fluid-011212-140721.

[53] S. Elgar, R. T. Guza, Observations of bispectra of shoaling surface gravity waves, J. Fluid Mech. 161 (1985) 425–448. doi:10.1017/S0022112085003007.

[54] S. Elgar, R. T. Guza, Nonlinear model predictions of bispectra of shoaling surface gravity waves, J. Fluid Mech. 167 (1986) 1–18. doi:10.1017/S0022112086002690.

[55] A. Toffoli, L. Cavaleri, A. V. Babanin, M. Benoit, E. M. Bitner-Gregersen, J. Monbaliu, M. Onorato, A. R. Osborne, C. T. Stansberg, Occurrence of extreme waves in three-dimensional mechanically generated wave fields propagating over an oblique current, Nat. Hazards Earth Syst. Sci. 11 (3) (2011) 895–903. doi:10.5194/nhess-11-895-2011.

[56] P. A. E. M. Janssen, Nonlinear four-wave interactions and freak waves, J. Phys. Oceanogr. 33 (4) (2003) 863–884. doi:10.1175/1520-0485(2003)33<863:NFIAFW>2.0.CO;2.

[57] I. R. Young, A. Babanin, The form of the asymptotic depth-limited wind-wave spectrum. Part II - The wavenumber spectrum, Coast. Eng. 56 (5-6) (2009) 534–542. doi:10.1016/j.coastaleng.2008.11.005.

[58] I. R. Young, The form of the asymptotic depth-limited wind-wave spectrum. Part III - Directional spreading, Coast. Eng. 57 (1) (2010) 30–40. doi:10.1016/j.coastaleng.2009.09.001.

[59] N. E. Huang, M.-L. C. Wu, S. R. Long, S. S. P. Shen, W. Qu, P. Gloersen, K. L. Fan, A confidence limit for the empirical mode decomposition and Hilbert spectral analysis, Proc. R. Soc. A Math. Phys. Eng. Sci. 459 (2037) (2003) 2317–2345. doi:10.1098/rspa.2003.1123.